RSC Advances

PAPER

View Article Online
View Journal | View Issue

Cite this: *RSC Adv.*, 2022, **12**, 14631

Yb-doped SnO_2 electron transfer layer assisting the fabrication of high-efficiency and stable perovskite solar cells in air†

Dixin Liu,‡[a] Wenyuan Zhang,‡[a] Ziqiu Ren*[b] and Xin Li *[a]

To date, most preparation processes of polycrystalline perovskite films still have to be performed in a glovebox filled with inert gas, limiting the application due to their high cost and complexity. In this work, we exploit a facile processing technique for the preparation of perovskite solar cells (PSCs) under ambient conditions by the Yb^{3+} doping effect for SnO_2 electron transfer layer. This remarkable and facile interface doping strategy promotes all-air processed planar PSCs, giving enhanced power conversion efficiency (PCE) from 15.69% to 17.31% with a decreasing hysteresis effect. Moreover, the heating and illumination stability of modified devices by virtue of defect suppression located at electron transfer layer (ETL)/perovskite interface has been effectively improved, retaining over 85% of its initial PCE after 7 h heating at 100 °C in ambient condition and 85% of its initial PCE under 7 h continuous light illumination without any encapsulation. Therefore, it is believed that this Yb-doping strategy for SnO_2 ETL can provide a novel way of promoting the efficiency and stability of devices prepared in the air.

Received 26th February 2022
Accepted 22nd April 2022

DOI: 10.1039/d2ra01297a

rsc.li/rsc-advances

Introduction

Organic–inorganic perovskite solar cell (PSC) has attracted extensive attention from scientists all over the world due to its excellent photovoltaic efficiency and solution processability,[1,2] where its power conversion efficiency (PCE) has rapidly increased from 3.8% to 25.5%, which is close to the best efficiency of single-junction silicon solar cells.[3,4] Despite the rapid improvement of recording efficiency, PSCs still face some challenges, such as lead toxicity, current–voltage (*J*–*V*) hysteresis, and device instability.[5–7] Particularly, the instability of perovskite materials and devices, including environmental, heating, and illumination instability has become a very thorny issue in practical application.[8,9] To address these issues, many advanced preparation technologies and strategies have been successively developed, among which the modification of the electron transfer layer (ETL)/perovskite interface is demonstrated to be the most reliable and effective method for optimizing interfacial defect and electronic structure.[10–12] Extensively documented defects located at the ETL/perovskite interface inevitably capture photo-induced electrons, leading to serious interface recombination in the device.[13–15] Meanwhile, interface defects and chemical structure can also easily give rise to perovskite decomposition and device degradation.[16,17] PCBM mixture layer has been used to passivate the defects and restrain the interfacial carrier recombination between the stannic oxide and perovskite interface.[18] 2-Mercaptoimidazole have been inserted between the hole transport layer and perovskite layer to form a cross-linking bridge.[19] An interfacial engineering strategy is developed to enlarge the grain size and enhance the crystallinity of the perovskite film by inserting a methylammonium chloride layer between the SnO_2 electron transport layer and perovskite layer.[20] It is reported that $(Li_3O)M(BH_4)_{3-x}Br_x$ has been introduced to modify the AMX_3-type perovskite.[21] Doping effect by metal ions on the ETL has been demonstrated to be an effective modification tactic to reduce the interface defects and accelerate the extraction of photo-induced electrons.[22,23] An Al-doped TiO_2 ETL has been developed to reduce the defects and enhance the conductivity, obtaining faster electron collection and less recombination in PSCs.[24] Also, it is demonstrated that Y^{3+} ions can modify the SnO_2/perovskite interface and block recombination in PSCs.[25] Especially, rare-earth (RE) ions serve as a kind of promising dopant, and a few rare-earth ions like La^{3+}, Nd^{3+}, and Er^{3+} have also been tentatively introduced to dope the ETL.[26–28] However, these works primarily focused on the regulation of electronic structure and efficiency promotion of the device. The rare-earth doping effects on the stability of perovskite devices, heating, and illumination stability in particular, have not yet received much attention, and more systematic studies are needed.

[a]*MIIT Key Laboratory of Critical Materials Technology for New Energy Conversion and Storage, School of Chemistry and Chemical Engineering, State Key Lab of Urban Water Resource and Environment, Harbin Institute of Technology, 150001 Harbin, China. E-mail: lixin@hit.edu.cn*

[b]*Henan Institute of Advanced Technology, Zhengzhou University, Zhengzhou 450052, P. R. China. E-mail: renziqiu@hit.edu.cn*

† Electronic supplementary information (ESI) available: Table S1 work function of SnO_2 and Yb-doped SnO_2 film. See https://doi.org/10.1039/d2ra01297a

‡ These authors contributed equally to this work.

Although the PCE has rapidly increased, most of the state-of-the-art preparation techniques of PSCs still have to operate in an inert-gas glovebox, consequentially increasing the fabrication cost.[29] Therefore, to escape its dependence on inert gas, all air-processed fabrication of PSCs has been exploited to simplify the process and reduce cost, more in line with the application demand in the future. The key points of all air-processed fabrication of PSCs are interfacial engineering and trap state density. Previously, we have developed some all-air fabrication strategies, including isopropanol-assisted crystallization, green antisolvent, and interface passivation of NH_4F.[30–32] However, the fabrication of stable and efficient devices in the air is still a huge challenge.

Herein, we report an effective method for fabricating stable and efficient PSCs in ambient conditions by applying Yb^{3+} as a dopant for the SnO_2 ETL in the planar PSC. Firstly, high-quality perovskite films can be easily obtained onto Yb-doped SnO_2 substrates even in ambient conditions with relatively high humidity and oxygen content. It is also proved that the passivation effect of Yb doping can effectively reduce the interface defects of SnO_2/perovskite, certainly expediting the extraction of electrons and suppressing the interface recombination of carriers. With a structure of F-doped SnO_2/Yb-doped SnO_2/$CH_3NH_3PbI_3$/spiro-OMeTAD/Au, the all air-processed device yields the highest PCE of 17.08%, which is much higher than 14.30% of control devices. More importantly, the heating and illumination stability of the optimized device has also been significantly enhanced, retaining over 85% PCE after 7 h heating at 100 °C and over 85% PCE after 7 h illumination (AM 1.5 G illumination, 1 sun). This Yb-doped SnO_2 ETL provides a new option for the preparation of stable and efficient PSCs in ambient air.

Experimental

Materials

Tin chloride pentahydrate and ytterbium(III) chloride were purchased from Aladdin Reagent (China). Other anhydrous solvents were obtained from Alfa Aesar. PbI_2, MAI 4-*tert*-butylpyridine, and lithium bis were purchased from Kanto. Spiro-OMeTAD was obtained from You Xuan Trade Co., Ltd., Yingkou, China. All chemicals and reagents were used as received without any further purification.

Preparation of Yb-doped SnO_2 nanoparticles

SnO_2 and Yb-doped SnO_2 are fabricated by a hydrothermal growth method. The solution was prepared by dissolving 0.1 mmol stannic chloride pentahydrate ($SnCl_4 \cdot 5H_2O$) and 1.5% mass fraction of ytterbium(III) chloride in 1 mL deionized water. Then, the solution was stirred under ambient conditions for 6 h at 70 °C.

Device fabrication

The conductive F-doped SnO_2 (FTO) substrates were cleaned successively with an abluent, deionized water, acetone, and UV–ozone to achieve a clean surface. After that, the ETL precursor was spin-coated onto the FTO substrates (500 rpm for 3 s, 3000 rpm for 30 s) and then heated at 180 °C for 1 h. The ETL substrates were treated with UV–ozone for 15 min before use. Perovskite precursor solution containing PbI_2 (1.1 M) and methylammonium iodide (MAI) (1.0 M) in a mixed solvent of DMF and DMSO (v/v = 4 : 1) was then spin-coated at 500 rpm for 3 s and then at 3000 rpm for 60 s. 300 μL of ethyl acetate (antisolvent) was dropped onto the spinning substrates at the first 16 s. After 25 min of annealing at 100 °C, shiny and dark brown perovskite films can be obtained. To prepare the HTL solution, 80 mg spiro-OMeTAD, 28.8 μL 4-*tert*-butylpyridine, and 17.4 μL Li–TFSi solution (520 mg in acetonitrile) were dissolved in 1 mL chlorobenzene, and then 50 μL HTL solution was spin-coated onto the perovskite layer at 3000 rpm for 20 s. Finally, 80 nm Au electrode was deposited *via* vacuum thermal evaporation. In this work, the planar devices with the structure of FTO/Yb-doped SnO_2/$CH_3NH_3PbI_3$/spiro-OMeTAD/Au were fabricated, measured, and stored totally in the air without any specific protection.

Characterization

X-ray diffractometer (XRD) patterns were collected on X-ray diffractometer (SHIMADU) with Cu Kα radiation (λ = 1.5418 Å). X-ray photoelectron spectroscopy (XPS) was carried out on a photoelectron spectrometer (PHI 5400 ESCA System, Al Kα). The current density–voltage data was collected through an electrochemical workstation with a scan rate of 0.2 V s^{-1} (VersaSTAT 3, Ametek, USA) under AM 1.5 G illumination (100 mW cm^{-2}, Newport 9402A) calibrated by a standard Si solar cell (1218, Newport, USA). The monochromatic incident photon-to-electron conversion efficiency (IPCE) was carried out by the Crowntech solar cell quantum efficiency measurement system (QTest station 500AD, USA) containing a monochromator, a chopper, a lock-in amplifier, and a multimeter (Keithley Model 2000). Photoluminescence (PL) spectra were measured by a fluorescence spectrometer (LS55 PerkinElmer, PE) with an excitation wavelength of 400 nm. Electrochemical impedance spectroscopy (EIS) was measured in the dark by the electrochemical workstation (VersaSTAT 3, Ametek, USA) with a bias of −0.9 V. The frequency range is 100 kHz to 0.1 Hz. The space-charge-limited current (SCLC) curves were measured under the linear sweep method with the voltage range from −5.0 V to 5.0 V by the electrochemical workstation (VersaSTAT 3, Ametek, USA).

Result and discussion

Characterization of SnO_2 ETL and perovskite films

The high quality SnO_2 ETL in PSCs should not only transport the photo-generated electrons effectively but also block the holes to reduce the carrier recombination. The surface of the SnO_2 layer has a significant effect on the morphology topography of the perovskite film, which is associated with the performance of PSCs.[33,34] In this work, SnO_2 has been prepared by hydrothermal synthesis and modified with ytterbium chloride solution (refer to the Experimental part for detail). By a one-step solution spin-coating method, the perovskite films have been coated onto SnO_2 and Yb-doped SnO_2 substrates in

ambient conditions. According to the SEM images shown in Fig. 1a and b, there are evident differences between the perovskite films on SnO_2 and Yb-doped SnO_2 ETL. Cracks can be formed among the perovskite crystalline coated onto the SnO_2 ETL, which would increase the risk of physical contact between ETL and HTL. It is gratifying that tightly arranged crystalline grains have been obtained in the perovskite film coated onto Yb-doped SnO_2. Compact and dense perovskite film is beneficial to efficiently convert light to electricity and decrease the non-radiative recombination, especially in the cracks of perovskite film. As shown in Fig. 1c–f, AFM images have also been collected to further observe the surface morphology of perovskite films. The surface roughness (RMS) value of perovskite films prepared on Yb-doped SnO_2 is 6.28 nm, which is smaller than that of perovskite films fabricated on SnO_2. It means that smoother perovskite film can be obtained onto the Yb-doped ETL, which is beneficial for constructing high-efficiency PSCs.

According to the XRD results of perovskite films on these two different SnO_2 substrates (Fig. 2a), there are characteristic diffraction peaks located at 14.1°, 23.4°, 24.5°, 28.5°, 31.6°, 40.4°, and 43.1°, corresponding to the (110), (211), (202), (220), (310), (224), and (314) lattice planes of tetragonal phase $CH_3NH_3PbI_3$, respectively.[35,36] Almost no difference can be found in the crystalline structure of perovskite, even on different SnO_2 substrates. As shown in Fig. 2b, the optical absorption of $MAPbI_3$ film on Yb-SnO_2 ETL is slightly enhanced in the range of 500–750 nm wavelength compared with that of the $MAPbI_3$ film on SnO_2 ETL. Both the absorption edges are located at around 800 nm, which matches well with the band gap of tetragonal $CH_3NH_3PbI_3$ (1.51 eV). To evaluate the doping effect of Yb, the surface chemical and electronic states of SnO_2 have been surveyed through XPS test, as shown in Fig. 3, which can act seriously on the carrier transfer and recombination processes in PSCs. As shown in Fig. 3a, Sn 3d and O 1s core electrons can be detected from the full XPS spectra of Yb-doped and undoped SnO_2 films. In order to reveal the successful introduction of Yb^{3+} ions, the XPS test results of SnO_2 films with and without Yb^{3+} ions are presented in Fig. 3b. The existence of a Yb 4d peak with weak intensity at 190.9 eV for the Yb-doped SnO_2 film indicates that a trace amount of Yb^{3+} ions is successfully introduced into the SnO_2 film.[37] XPS test can also be used as an effective technique to figure out these oxygen-induced defects in SnO_2. In Sn 3d XPS spectra of both samples (Fig. 3c and d), the Sn $3d_{3/2}$ peak at 496.0 and Sn $3d_{5/2}$ peak at 486.6 eV are identified in agreement with tetravalent tin. The O 1s XPS spectra of undoped SnO_2 and Yb-doped SnO_2 are shown in Fig. 3e and f, which can be attributed to two O chemical states at 529.2 eV and 530.7 eV. The O 1s peak with a binding energy of 529.2 eV corresponds to the O–Sn–O bond (denoted as O_{Sn-O}), while the peak at 530.7 eV can be attributed to the oxygen vacancy (denoted as O_V). Based on the peak area

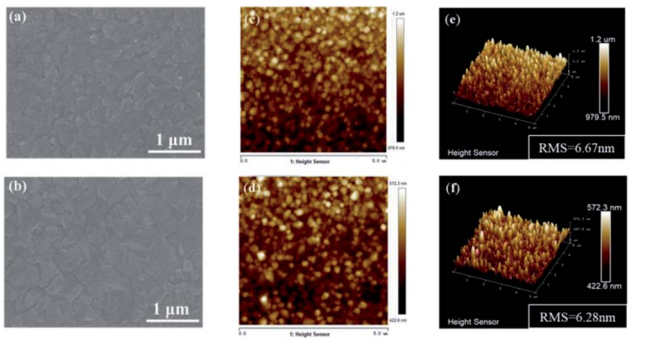

Fig. 1 SEM images of perovskite films spin-coated on (a) SnO_2 substrates and (b) Yb-doped SnO_2 substrates, AFM images of perovskite films spin-coated on (c) SnO_2 substrates and (d) Yb-doped SnO_2 substrates, the surface roughness (RMS) of perovskite films spin-coated on (e) SnO_2 substrates and (f) Yb-doped SnO_2 substrates.

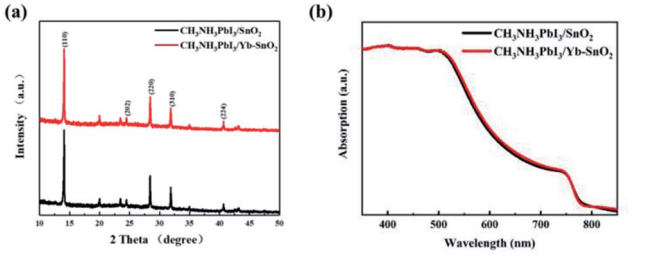

Fig. 2 (a) XRD patterns of perovskite films on pristine SnO_2 and Yb-doped SnO_2 film. (b) UV-Vis spectra of perovskite films on SnO_2 and Yb-SnO_2 ETLs, respectively.

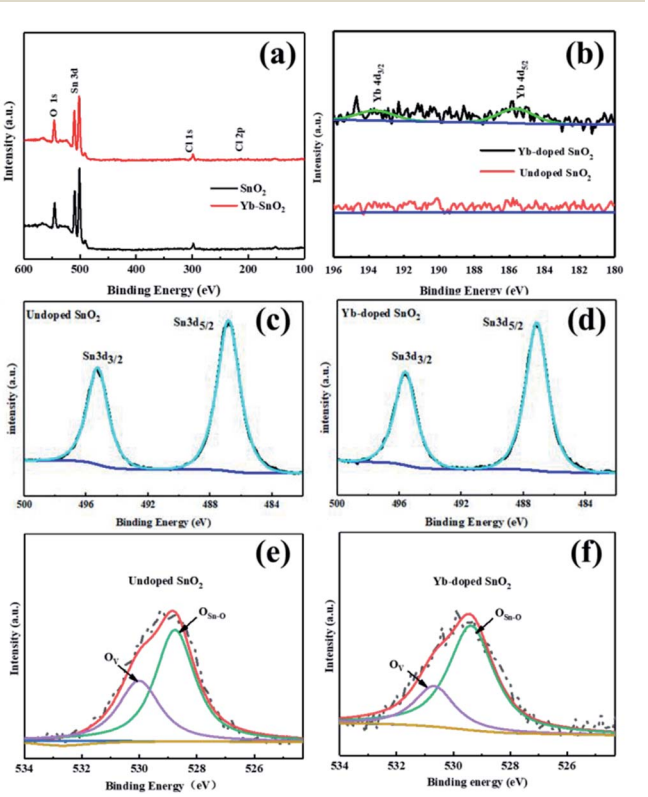

Fig. 3 Full XPS spectra of (a) the undoped SnO_2 film and Yb-doped SnO_2 film, (b) the Yb 4d of the SnO_2 film and Yb-doped SnO_2 film, (c) the Sn 3d of undoped SnO_2, (d) the Sn 3d of Yb-doped SnO_2, (e) the O 1s of undoped SnO_2, and (f) the O 1s of Yb-doped SnO_2.

ratios of O_{Sn-O} and O_V, the relative amount of each O state in the whole O 1s (O_{Sn-O} + O_V) can be estimated (Table 1), among which the oxygen vacancy reflecting the oxygen-induced defect is closely related to the carrier transport and recombination. It turns out that the O_V decreased from 30.47% for the pure SnO_2 to 25.51% for Yb-doped SnO_2. The oxygen-induced defects situated at the interface of SnO_2 and perovskite may lead to the enhanced transport of the photo-generated carriers.[38,39]

Photovoltaic performance

Planar devices with FTO/Yb-doped SnO_2 ETL/$CH_3NH_3PbI_3$/spiro-OMeTAD/Au structure have been successfully constructed in air. To evaluate the photovoltaic parameters (AM 1.5 G illumination, 1 sun), the forward and reverse *J–V* curves of the control and Yb-doped devices have been collected and shown in Fig. 4a, and the photovoltaic parameters, including PCE, V_{oc}, J_{sc}, and FF are summarized in Table 2. The champion device based on control SnO_2 presents a PCE of 15.69% with a V_{oc} of 1.03 V, a J_{sc} of 20.55 mA cm^{-2}, and a FF of 74.13% under the reverse scan, while the champion device with Yb achieves a more superior PCE of 17.31% with a J_{sc} of 21.85 mA cm^{-2}, a V_{oc} of 1.06 V, and a FF of 74.40%. It is clear that the V_{oc} and PCE have been improved significantly with the addition of Yb. More notably, the hysteresis index (HI = ($PCE_{reverse}$ − $PCE_{forward}$)/$PCE_{reverse}$) of Yb-SnO_2-based device is reduced to 3.52%, compared to 9.88% of the control SnO_2 device. It has been found that interface defects and charge accumulation are important factors causing hysteresis.[40] Thus, the lower HI of the Yb-SnO_2 device reflects that Yb dopants can effectively promote charge transport and can effectively reduce interface defects, which is confirmed by PL and time-resolved photoluminescence (TRPL). The hysteresis of *J–V* curves for the Yb-doped device is smaller than that of the SnO_2 device. It has been found that the hysteresis effect is associated with the interfacial defects and quality of perovskite films.[41,42] As demonstrated in the SEM and AFM images, the smoother perovskite film and larger grains can be obtained easily onto the Yb-doped SnO_2 ETL. Additionally, the oxygen-induced defects located at the ETL/perovskite interface have been decreased successfully by Yb doping, which would accelerate the extraction of photo-induced electrons and suppress the recombination of carriers at the interface.[43] Moreover, the hysteresis effect of *J–V* curves under forward and reverse scanning for the optimized device has also been significantly alleviated compared with the control device. In addition to the interface defects, the interfacial electric field, especially built-in potential in the device, is also closely related to the carrier transport and recombination, which can be speculated from the surface potential changes of SnO_2 films tested by scanning Kelvin probe microscopy (SKPM).[44] According to the test results in Table S1,† the surface work function values of SnO_2 and Yb-SnO_2 have been estimated. After Yb doping, the work function of SnO_2 drops slightly from 4.28 eV to 4.17 eV. As described in the literature, the decrease in the work function of ETL always corresponds to the enhancement of built-in potential in the device.[45] This enhanced built-in potential can not only speed up electron extraction but also make the detrapping of electrons, consequently suppressing the interface recombination caused by the defects.[46] This enhanced built-in potential is reflected in the open-circuit voltage improvement of Yb-doped devices according to the above *J–V* results. The hysteresis in the *J–V* measurement leads to the instability of devices, which seriously hinders the application of PSCs. As reported, ion migration, defects at the interface, and accumulated unbalanced charge carriers are the three main sources of hysteresis in PSCs.[47,48] In the optimized devices, the

Table 1 Peak position, area, and area ratio of O_{Sn-O}, O_V, O_{O-H}, for the undoped SnO_2 and Yb-doped SnO_2

O 1s		Undoped SnO_2	Yb-doped SnO_2
O_{Sn-O}	Position (eV)	529.14	529.37
	Area	3368.06	1746.12
O_V	Position (eV)	530.16	530.67
	Area	1475.89	598.07
O_{Sn-O}	Area ratio (%)	69.53	74.49
O_V	Area ratio (%)	30.47	25.51

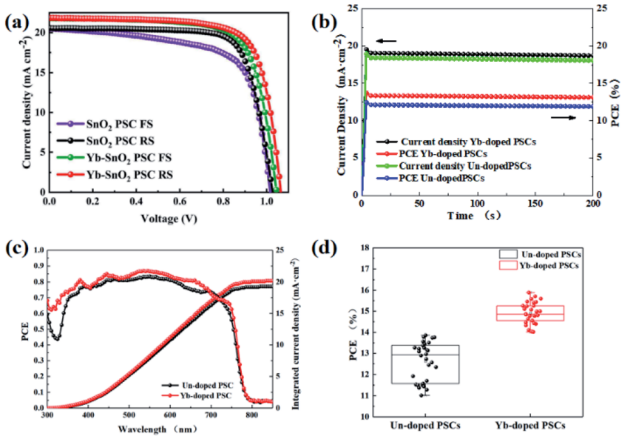

Fig. 4 (a) *J–V* curves with forward and reverse scan under the 0.2 V s^{-1} scan rate, (b) steady-state photocurrent density and power outputs, (c) IPCE spectra, (d) PCE histograms of PSCs.

Table 2 Champion performance of SnO_2 device and Yb-doped based device

Type	J_{sc} (mA cm^{-2})	V_{oc} (V)	FF (%)	PCE (%)
SnO_2 device reverse	20.55	1.03	74.13	15.69
SnO_2 device forward	20.51	1.02	67.88	14.14
Yb-doped SnO_2 device reverse	21.85	1.06	74.40	17.31
Yb-doped SnO device forward	21.81	1.05	73.23	16.70

defect passivation of SnO_2/perovskite interface and removal of residual hydroxyl will undoubtedly accelerate the interface electron extraction, leading to the reduction of hysteresis effect. As shown in Fig. 4c, IPCE spectra of the control and optimized devices show the same light-response range from 300 nm to 850 nm. The IPCE value of the optimized device is about 75–85%, which is higher than the 60–70% of the control device. According to the IPCE spectra, the integral current of 19.30 mA cm^{-2} for the original device and 20.20 mA cm^{-2} for the optimized device can be calculated, which is consistent with the *J–V* testing results. To evaluate the operating stability of the devices, 200 s maximum power point tests have been carried out (Fig. 4b), indicating both devices show a stable power output. However, the saturation time for the Yb-doped device is shorter than that of the SnO_2 device. The faster carrier separation and extraction profited by the enhanced built-in potential in the optimized device leads to the quicker climbing to the maximum power point. In addition, the PCEs of 30 control or optimized devices have been independently collected to plot the histogram. As shown in Fig. 4d, the *J–V* curves of the control and Yb-doped devices have been collected and shown in Fig. 4d and S1–S3,† and the average photovoltaic parameters, including PCE, V_{oc}, J_{sc}, and FF are summarized in Table S2.† The average parameters of devices based on control SnO_2 present a PCE of 12.63%, with a V_{oc} of 0.98 V, a J_{sc} of 19.12 mA cm^{-2}, and a FF of 67.16%, while average parameters of Yb-doped devices present a more superior PCE of 14.92% with a J_{sc} of 20.24 mA cm^{-2}, a V_{oc} of 1.01 V, and a FF of 72.60%. The PCEs of optimized devices are distributed in the range of 14–16%, which is better than the control devices at 11–14%.

Carrier transport and recombination

According to PL intensity of perovskite at different substrates (FTO, SnO_2/FTO, and Yb-doped SnO_2/FTO, Fig. 5a), the electronic extraction ability of ETL in PSCs can be evaluated. The weaker intensity in PL means the stronger electron extraction ability of ETLs.[49] In general, defects or traps in the crystal structure cause quenching of PL,[50] which lead to a reduced PL intensity and a shortened PL lifetime of photogenerated carriers in the absorber layer because it is an additional nonradiative de-excitation path for carriers. Here, the enhancement of PL intensity and growth of fluorescence lifetime implies that Yb^{3+} processed interface between ETL and perovskite film can effectively reduce the densities of traps, thereby decreasing the nonradiative recombination of carriers. Compared with the PL intensity of perovskite film on the FTO substrate, the perovskite film onto SnO_2 ETL reveals an obvious quenching effect in the PL spectra. It is worth noting that Yb-doped SnO_2, as an ETL, has a stronger quenching effect compared with the original SnO_2, which means that photoinduced electron extraction of Yb-doped SnO_2 ETL is more efficient. Furthermore, the TRPL results in Fig. 5b also further confirm that this Yb-doped SnO_2 ETL has better electron extraction capability. It is generally believed that faster electron extraction in the optimized device can reduce the risk of electron accumulation and recombination at the ETL/perovskite interface. In order to study the recombination of carriers in photovoltaic devices, dark EIS has been measured within the frequency range of 0.1 Hz to 100 kHz. According to the Nyquist plots (Fig. 5c), only one semicircle is presented identical to that reported in the literature,[51] of which the equivalent circuit has been inserted in Fig. 5c. The recombination resistances in control and optimized devices can be estimated by the size of the semicircle, and the larger one means the bigger the recombination resistance.[52,53] Obviously, the optimized device shows a bigger recombination resistance. As demonstrated above, defect passivation and enhanced built-in potential can suppress carrier recombination at the SnO_2/perovskite interface. To further understand the trap density of SnO_2 ETL, space-charge-limited current (SCLC) measurements of FTO/SnO_2 or Yb-doped SnO_2/perovskite/PCBM/Au devices are carried out (Fig. 5d). In the range of low bias voltages, the linear relationship (black and orange line) of current and voltage represents the ohmic response of electron-only devices. When the bias voltage exceeds the kink point (trap-filled limit, TFL), the current rapidly increases nonlinearly (green and pink line), suggesting that the trap state is completely filled by the injected carriers. At high fields, the current showed a quadratic voltage dependence in the Child's regime (yellow line). The trap density (N_t) can be calculated by the trap-filled limit voltage (VTFL) using eqn (1).

$$V_{TFL} = \frac{eN_tL^2}{2\varepsilon\varepsilon_0} \quad (1)$$

where e is the elementary charge of the electron, N_t is the trap-state density, L is the thickness of perovskite film, ε is the relative dielectric constant of $MAPbI_3$ ($\varepsilon = 32$), and ε_0 is the vacuum permittivity. The V_{TFL} of the perovskite films is reduced from 0.71 V of pure SnO_2 to 0.27 V with Yb-doped SnO_2, corresponding to the N_t of 1.57×10^{16} cm^{-3} and 5.98×10^{15} cm^{-3}, respectively. The lower trap density is attributed to the smoother interface, which helps to increase the contact between perovskite and the Yb-SnO_2 ETL layer. The above

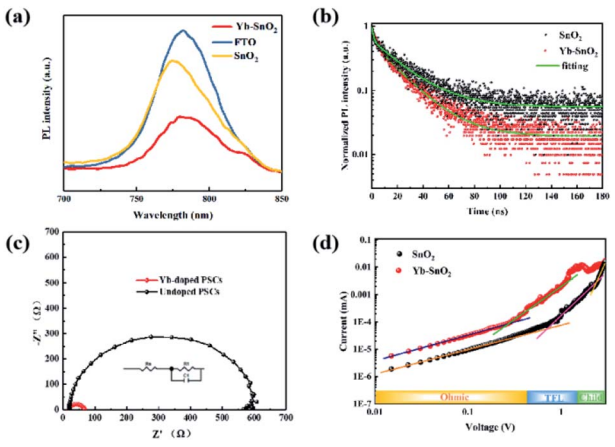

Fig. 5 (a) PL and (b) TRPL spectra of perovskite films onto FTO/SnO_2 FTO/Yb-doped SnO_2, (c) Nyquist plots of pristine PSC and Yb-PSC acquired from the dark EIS measurement under a bias of −0.9 V, (d) SCLC curves for the device of FTO/pristine SnO_2 or Yb-doped SnO_2/perovskite/PCBM/Au.

characterization results all indicate that SnO_2 has been effectively passivated by Y doping, resulting in less recombination and faster transfer of the photon-generating carriers in the device. This passivation of defects in SnO_2 can remove the obstacles in the process of electron transport and the accumulation of interface charges.

We further used steady-state PL and TRPL to analyze the charge generation and recombination kinetics of perovskite films deposited on different ETLs substrates (Fig. 5b). The PL intensity of FTO/Yb-SnO_2/perovskite film is obviously lower than that of the FTO/SnO_2/perovskite, indicating more effective electron extraction and transfer. This may be due to the better interface between the perovskite layer and the SnO_2 layer, meanwhile, the TRPL curves are fitted by a biexponential decay function, given as eqn (2):

$$y = y_0 + \sum A_i \exp\left[\frac{-(x - x_0)}{\tau_i}\right] \quad (2)$$

where A_i is the decay amplitude and τ_i is the PL decay time. The average PL decay lifetime (τ_{ave}) is evaluated by the A_i and τ_i values using eqn (3). The corresponding detailed parameters are summarized in Table 3.

$$\tau_{ave} = \frac{\sum A_i \tau_i^2}{\sum A_i \tau_i} \quad (3)$$

The result shows that the τ_{ave} of SnO_2-based perovskite film is 22.38 ns, while that of Yb-doped SnO_2-based perovskite film is merely 3.3 ns. In addition, the ratio of τ_1 is far outweighing than that of τ_2. It suggests that a faster electron transfer occurs at the interface of Yb-doped SnO_2/perovskite film, which can effectively reduce the accumulation of charge at the interface, so it is expected to extremely reduce the device hysteresis.

Stability

The instability of PSCs is one of the biggest challenges in practical applications due to the fragile perovskite material, which breaks down easily in case of moisture, oxygen, heating, and illumination. Through appropriate encapsulation, the perovskite device can avoid getting in touch with moisture and oxygen.[54] However, the instability of perovskite material under heating and illumination is difficult to solve only by encapsulation, which has become a bottleneck that impedes the practical application of PSC.[55] Although 85 °C is the common testing temperature for photovoltaic panels,[56] we measured PSCs at 100 °C to accelerate ageing within a short time. As shown in Fig. 6a and b, the heating and illumination stability of control and optimized devices were tested in the air without any encapsulation. According to the 100 °C-heating test results, the optimized devices can maintain 83% of the original PCE after 7 hour heating, of which photovoltaic parameters remain relatively stable. However, the PCE of the control device drops dramatically to less than 15% of the original value after 4 hour heating. The sharp decline of FF, V_{oc} and J_{sc} all indicate the serious degradation of the devices. Similarly, the optimized devices under illumination also reveal stable output, showing more than 80% original PCE value even after 7 hour illumination (Fig. 6b). By contrast, the degradation of control devices under illumination is even more pronounced. As demonstrated above, the introduction of Yb^{3+} can reduce the oxygen vacancy concentration of SnO_2/perovskite interface, which is the active site of perovskite decomposition, especially under illumination. As displayed in Fig. S4,† the PCE of the Yb-doped SnO_2 device maintains 90.25% of the original PCE after 28 days, and by contrast, the SnO_2 device only maintains 46.60%. Obviously, the Yb-doped SnO_2 device shows better air long-term stability. Similarly, Yb^{3+} ions also play a positive role in reducing interface trap states and inhibiting the degradation of perovskite films. Finally, stable planar PSCs can be prepared in air efficiently through this simple interface modification.

Table 3 Values for TRPL characteristics of perovskite films deposited on Yb-SnO_2 and SnO_2

ETL	τ_{ave} (ns)	τ_1 (ns)	A_1	τ_2 (ns)	A_2
SnO_2	22.38	1.15	0.47	23.28	0.55
Yb-SnO_2	19.08	2.78	0.34	20.53	0.52

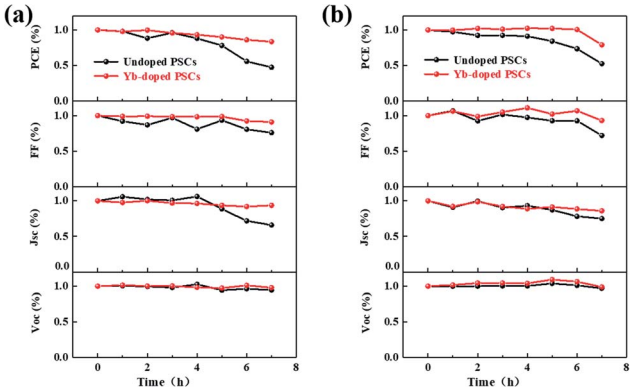

Fig. 6 (a) Thermostability (heating at 100 °C) and (b) illumination stability (AM 1.5 G illumination, 100 mW cm^{-2}) tests of control and optimized devices.

Conclusion

In conclusion, we studied the Yb-doping effect on the morphology, electrical, and optical properties of SnO_2 ETL and demonstrated the improvement of device efficiency and stability *via* this doping strategy. High-quality large-grain perovskite films have been successfully prepared on Yb-doped SnO_2 ETL and the planar devices of FTO/Yb-doped SnO_2/$CH_3NH_3PbI_3$/spiro-OMeTAD/Au have been assembled in air. The interface defects in the optimized device have been suppressed effectually, accelerating the extraction of photo-induced electrons and inhibiting the nonradiative recombination in the device. Finally, the champion device with an ETL of Yb-doped SnO_2 yields a PCE of 17.31%, which is much higher than the 15.69% PCE of the control device. Furthermore, the decrease of oxygen vacancy in the optimized device can lessen the risks of

perovskite decomposition and promote device stability. It is noticed particularly that heating and illumination stabilities of optimized devices have also been improved markedly, which is of significant meaning in future applications, considering the all air-processed fabrication.

Conflicts of interest

There are no conflicts to declare.

Acknowledgements

This work is supported by the Natural Science Foundation of Heilongjiang Province of China (LH2021E054).

References

1 L. Etgar, P. Gao, Z. Xue, Q. Peng, A. K. Chandiran, B. Liu, M. K. Nazeeruddin and M. Grätzel, *J. Am. Chem. Soc.*, 2012, **134**, 17396–17399.
2 A. Polman, M. Knight, E. C. Garnett, B. Ehrler and W. C. Sinke, *Science*, 2016, **352**, aad4424.
3 A. Kojima, K. Teshima, Y. Shirai and T. Miyasaka, *J. Am. Chem. Soc.*, 2019, **131**, 6050–6051.
4 S. Wang, Y. Jiang, E. J. Juarez-Perez, L. K. Ono and Y. B. Qi, *Nat. Energy*, 2016, **2**, 16195.
5 Z. Xiao, Z. Song and Y. Yan, *Adv. Mater.*, 2019, **31**, 1803792.
6 Q. Fan, G. V. Biesold-McGee, J. Ma, Q. Xu, S. Pan, J. Peng and Z. Lin, *Angew. Chem., Int. Ed. Engl.*, 2020, **59**, 1030–1046.
7 B. W. Park and S. I. Seok, *Adv. Mater.*, 2019, **31**, 1805337.
8 R. Wang, M. Mujahid, Y. Duan, Z.-K. Wang, J. Xue and Y. Yang, *Adv. Funct. Mater.*, 2019, **29**, 1808843.
9 Y. Zhou and Y. Zhao, *Energy Environ. Sci.*, 2019, **12**, 1495–1511.
10 T. H. Han, S. Tan, J. Xue, L. Meng, J. W. Lee and Y. Yang, *Adv. Mater.*, 2019, **31**, 1803515.
11 A. K. Jena, A. Kulkarni and T. Miyasaka, *Chem. Rev.*, 2019, **119**, 3036–3103.
12 H. D. Pham, X. Q. Li, W. H. Li, S. Manzhos, A. K. K. Kyaw and P. Sonar, *Energy Environ. Sci.*, 2019, **12**, 1177–1209.
13 D. Luo, R. Su, W. Zhang, Q. Gong and R. Zhu, *Nat. Rev. Mater.*, 2020, **5**, 44–60.
14 J. Chen and N. G. Park, *Adv. Mater.*, 2019, **31**, 1803019.
15 L. K. Ono, S. Liu and Y. Qi, *Angew. Chem., Int. Ed.*, 2020, **59**, 6676–6698.
16 S. Singh, L. Laxmi and D. Kabra, *J. Phys. D: Appl. Phys.*, 2020, **53**, 503003.
17 E. Aydin, M. De Bastiani and S. De Wolf, *Adv. Mater.*, 2019, **31**, 1900428.
18 X. Hu, H. Wang, M. Wang, *et al.*, *Sol. Energy*, 2020, **206**, 816–825.
19 M. Wang, W. Li, H. Wang, *et al.*, *Adv. Electron. Mater.*, 2020, 2000604.
20 X. Hu, H. Wang, Y. Ying, *et al.*, *J. Power Sources*, 2020, **480**, 229073.
21 T. Zhou, Y. Zhang, M. Wang, *et al.*, *J. Power Sources*, 2019, **429**, 120–126.
22 X. D. Ren, D. Yang, Z. Yang, J. S. Feng, X. J. Zhu, J. Z. Niu, Y. C. Liu, W. G. Zhao and S. F. Liu, *ACS Appl. Mater. Interfaces*, 2017, **9**, 2421–2429.
23 Y. Lv, H. Tong, W. Cai, Z. Zhang, H. Chen and X. Zhou, *J. Alloys Compd.*, 2021, **851**, 156785.
24 S. K. Pathak, A. Abate, P. Ruckdeschel, B. Roose, K. C. Godel, Y. Vaynzof, A. Santhala, S. I. Watanabe, D. J. Hollman, N. Noel, A. Sepe, U. Wiesner, R. Friend, H. J. Snaith and U. Steiner, *Adv. Mater.*, 2014, **24**, 6046–6055.
25 P. Qin, A. L. Domanski, A. K. Chandiran, R. Berger, H. J. Butt, M. I. Dar, T. Moehl, N. Tetreault, P. Gao, S. Ahmad, M. K. Nazeeruddin and M. Grätzel, *Nanoscale*, 2014, **6**, 1508–1514.
26 X. X. Gao, Q. Q. Ge, D. J. Xue, J. Ding, J. Y. Ma, Y. X. Chen, B. Zhang, Y. Feng, L. J. Wan and J. S. Hu, *Nanoscale*, 2016, **8**, 16881–16885.
27 B. Roose, K. C. Gödel, S. Pathak, A. Sadhanala, J. P. C. Baena, B. D. Wilts, H. J. Snaith, U. Wiesner, M. Grätzel, U. Steiner and A. Abate, *Adv. Energy Mater.*, 2016, **6**, 1501868.
28 Z. Ren, J. Wu, N. Wang and X. Li, *J. Mater. Chem. A*, 2018, **6**, 15348–15358.
29 Y. H. Cheng, F. So and S. W. Tsang, *Mater. Horiz.*, 2019, **6**, 1611–1624.
30 W. Y. Zhang, Y. C. Li, X. Liu, D. Y. Tang, X. Li and X. Yuan, *Chem. Eng. J.*, 2020, **379**, 9.
31 Z. Ren, M. Zhu, X. Li and C. Dong, *J. Power Sources*, 2017, **363**, 317–326.
32 Z. Ren, N. Wang, M. Zhu, X. Li and J. Qi, *Electrochim. Acta*, 2018, **282**, 653–661.
33 G. Yang, C. L. Wang, H. W. Lei, X. L. Zheng, P. L. Qin, L. B. Xiong, X. Z. Zhao, Y. F. Yan and G. J. Fang, *J. Mater. Chem. A*, 2017, **5**, 1658–1666.
34 M. Yu, Y. R. Guo, S. Yuan, J. S. Zhao, Y. J. Qin and X. C. Ai, *RSC Adv.*, 2020, **10**, 12347–12353.
35 T. Baikie, Y. Fang, J. M. Kadro, M. Schreyer, F. Wei, S. G. Mhaisalkar, M. Graetzel and T. J. White, *J. Mater. Chem. A*, 2013, **1**, 5628–5641.
36 A. M. A. Leguy, Y. Hu, M. Campoy-Quiles, M. I. Alonso, O. J. Weber, P. Azarhoosh, M. van Schilfgaarde, M. T. Weller, T. Bein, J. Nelson, P. Docampo and P. R. F. Barnes, *Chem. Mater.*, 2015, **27**, 3397–3407.
37 S. H. Liang, D. F. Zhang, X. T. Yao, R. T. Han, Q. D. Zhang, C. Y. Jin, X. P. Pu and Y. L. Geng, *Sep. Purif. Technol.*, 2020, **238**, 116399.
38 Q. Sun, P. Fassl, D. Becker-Koch, A. Bausch, B. Rivkin, S. Bai, P. E. Hopkinson, H. J. Snaith and Y. Vaynzof, *Adv. Energy Mater.*, 2017, **7**, 1700977.
39 N. Aristidou, C. Eames, I. Sanchez-Molina, X. N. Bu, J. Kosco, M. S. Islam and S. A. Haque, *Nat. Commun.*, 2017, **8**, 15218.
40 P. Liu, W. Wang, S. Liu, H. Yang and Z. Shao, *Adv. Energy Mater.*, 2019, **9**, 180301713.
41 J. M. Azpiroz, E. Mosconi, J. Bisquert and F. De Angelis, *Energy Environ. Sci.*, 2015, **8**, 2118–2127.
42 X. J. She, C. Chen, G. Divitini, B. Zhao, Y. Li, J. Wang, J. F. Orri, L. Cui, W. Xu, J. Peng, S. Wang, A. Sadhanala and H. Sirringhaus, *Nat. Electron.*, 2020, **3**, 694–703.

43 C. T. Lin, F. De Rossi, J. Kim, J. Baker, J. Ngiam, B. Xu, S. Pont, N. Aristidou, S. A. Haque, T. Watson, M. A. McLachlan and J. R. Durrant, *J. Mater. Chem. A*, 2019, **7**, 3006–3011.
44 Z. Q. Ren, N. Wang, P. C. Wei, M. H. Cui, X. Li and C. C. Qin, *Chem. Eng. J.*, 2020, **393**, 9.
45 W. Zhang, Z. Ren, G. Yan, *et al.*, *Electrochim. Acta*, 2018, **268**, 539–545.
46 G. Yang, C. Wang, H. Lei, X. Zheng, P. Qin, L. Xiong, X. Zhao, Y. Yan and G. Fang, *J. Mater. Chem. A*, 2017, **5**, 1658–1666.
47 E. L. Unger, E. T. Hoke, C. D. Bailie, W. H. Nguyen, A. R. Bowring, T. Heumuller, M. G. Christoforo and M. D. McGehee, *Energy Environ. Sci.*, 2014, **7**, 3690–3698.
48 H. J. Snaith, A. Abate, J. M. Ball, G. E. Eperon, T. Leijtens, N. K. Noel, S. D. Stranks, J. T. W. Wang, K. Wojciechowski and W. Zhang, *J. Phys. Chem. Lett.*, 2014, **5**, 1511–1515.
49 Q.-D. Dao, A. Fujii, R. Tsuji, Y. Takeoka and M. Ozaki, *Org. Electron.*, 2017, **43**, 156–161.
50 W. Zhang, Y. Li, *et al.*, *Chem. Eng. J.*, 2019, **379**, 122298.
51 G. Niu, W. Li, F. Meng, L. Wang, H. Dong and Y. Qiu, *J. Mater. Chem. A*, 2014, **2**, 705–710.
52 J. A. Christians, R. C. M. Fung and P. V. Kamat, *J. Am. Chem. Soc.*, 2014, **136**, 758–764.
53 H. M. Yi, D. Wang, M. A. Mahmud, F. Haque, M. B. Upama, C. Xu, L. P. Duan and A. Uddin, *ACS Appl. Energy Mater.*, 2018, **1**, 6027–6039.
54 Y. Han, S. Meyer, Y. Dkhissi, K. Weber, J. M. Pringle, U. Bach, L. Spiccia and Y. B. Cheng, *J. Mater. Chem. A*, 2015, **3**, 8139–8147.
55 X. D. Li, S. Fu, S. Y. Liu, Y. L. Wu, W. X. Zhang, W. J. Song and J. F. Fang, *Nano Energy*, 2019, **64**, 103962.
56 C. C. Boyd, R. Cheacharoen and T. Leijtens, *Chem. Rev.*, 2019, **119**, 3418–3451.